Supporting Information

Nury et al. 10.1073/pnas.1001832107

SI Text

Full Methods. ***Crystallography.*** Several datasets of frozen single crystals were collected at the European Synchrotron Radiation Facility and at Soleil Synchrotron and processed with XDS (1) and CCP4 programs (2). Crystals are isomorphous to the wild-type ones; the space group is C2. Using the best dataset, a Fourier difference Fo-Fc map was calculated, which showed clear densities at the position of the mutation. The model was built with Coot (3) and refined with Refmac (4) and Buster (5) taking advantage of the targeted refinement module. Noncrystallographic symmetry restraints were applied. Molprobity (6) was used to validate the geometry: The overall score ranks our structure in the 93th percentile among structures of comparable resolution, the clashscore is 15.51 (96th percentile), and 0.32% of residues are outliers in the Ramachandran plot. Data collection and refinement statistics are given in Table S2.

An interesting side effect of the mutation is that the detergent bound in the pore in the wild-type structure is pushed out in the A13′F structure. The phenylalanine side chains within the pore lumen prevent the 6 detergent bundle formation. Residual densities in the Fourier difference maps could tentatively be attributed to partly disordered detergent molecules at the very top of the pore.

Molecular dynamics (MD). We used our previously published 20-ns-long molecular dynamics simulation of a full atomistic model of the *Gloeobacter violaceus* receptor (GLIC) with all hydrogens present at acidic pH 4.6 as the starting point (7). In this model, GLIC was inserted in a fully hydrated and neutralized palmitoyl-2-oleoyl-sn-glycerol-phosphatidylcholine lipid bilayer (307 lipids, 43,992 water molecules, and 54 Na^+ and 89 Cl^- ions) with a system size of 108 Å × 106 Å × 168 Å dimension. The detailed setup is described below. In order to represent the change in pH related to gating of the channel, we started from the equilibrated pH 4.6 simulation after 20 ns and assigned standard deprotonated states for pH 7 to all acidic side chains. This adds 55 negative charges to the channel and the same number of Cl^- ions was removed in order to maintain overall neutrality of the simulation system. The resulting balance in charge is the following: at acidic pH, 54 Na^+, 89 Cl^- and protein with a charge of +35, corresponding to an ionic strength of 0.09 molal; at neutral pH, 54 Na^+, 34 Cl^- and protein with a charge of −20, corresponding to an ionic strength of 0.06 molal.

In the initial pH 4.6 setup, the net charge of the system was neutralized with counterions, achieving a salt concentration of 100 mM. These steps were carried out within VMD (8), using the *membrane, solvate, and autoionize* plug-ins. All subsequent simulations were carried out with NAMD (9) using the CHARMM27 force field (10). Two rounds of equilibration were run, first with the protein fixed (600,000 steps) and then with restraints that were gradually released (2,500,000 steps). This was followed by a first 20-ns production run at pH 4.6. The pH change was operated as described above and the main 1.06-μs production run at neutral pH was carried out. All simulations were carried out at 310 K using Langevin dynamics. A Langevin piston algorithm was used to maintain the pressure at 1 atm. A short 10-Å cutoff was used for nonbonded interactions. Long-range electrostatic interactions were treated using the particle mesh Ewald method (11). The reversible reference system propagation algorithm multiple time step method (12) was employed with a 2-fs time step for bonded and for short-range nonbonded interactions, and a 4-fs step for long-range electrostatic forces. All bonds between hydrogens and heavy atoms were constrained with the SHAKE algorithm.

All MD simulations were carried out at the Institut du développement et des resources en informatique scientifique Supercomputer Center in Orsay (http://www.idris.fr), either on the machine Babel, an IBM Blue Gene/P, or the machine Vargas, an IBM Power 6 supercomputer. These high-performance computing resources were provided by Grand Equipement National de Calcul Intensif Institut du développement et des resources en informatique scientifique.

Control simulations. We performed 12 control simulations.

The first one, called O1, is a 50-ns-long extension of the open state simulation at pH 4.6.

Simulations P1–P11 are short 20-ns runs similar to the production run at pH 7.0, but in each simulation only one residue (along with its four symmetry-related mates) undergoes the change in protonation state. Those residues are E26, E35, E67, E69, E75, E82, D86, D88, E177, E253, and H277 for simulations P1 to P11, respectively. See Fig. S1 and Table S1 for more details on protonation states. These simulations show a wide range of effects (quantified by various rmsd) depending on the position of the residue changing charge, thereby limiting the possibility of a systematic effect due to the abrupt change of charges.

Trajectory analysis. Trajectories were visualized with VMD (8). Statistical and data analysis was performed using the R statistical software package (13). Figures were prepared with VMD and Pymol (14).

z-sliced twist angles.
(Fig. 3*C*) The protein was divided into ten slices perpendicular to its symmetry axis (*z* axis). The very top and very bottom were excluded so that each slice comprises a comparable number of atoms. For each subunit, the projections of the vector between the instantaneous molecular center of mass (of core carbon alpha atoms) and the subunit center of mass (non-hydrogen atoms) were averaged over a period of 100 ns. The cylindrical coordinate theta of the resulting vector was calculated in a referential where theta = 0 is defined by the initial position of the subunit's center of mass. Theta values were then averaged over subunits for each time interval. The twist angle increases almost linearly from the cytoplasmic side of the channel up to about the first third of the extracellular domain (ECD), remaining nearly constant above this region, with the hydrophobic gate marking the neutral point. Twist increases regularly throughout the simulation. When subunits are considered separately, the twist is still observed, but is asymmetric; the altitude of the neutral point as well as the altitude of the maximum twist vary (data not shown).

M2 helix trajectory.
(Fig. 4*A*) For each subunit i we considered the Cα of residues 221–241, corresponding to the part of M2 that conserves its topology throughout the simulation. We computed the center of mass CG_i and principal axis of inertia ν_i. We defined subunit-specific frames, centered on every CG_i, and characterized by 3 axes: Z_i parallel to the protein symmetry axis, X_i pointing toward the center of mass of all 5 centers of mass, and Y_i defined such as to obtain an orthonormal frame. This frame definition allows us to define polar, δ_i, and azimuthal, θ_i, angles that are readily comparable from one subunit to the other. The polar angle is defined as the angle between ν_i and Z_i. The azimuthal angle is defined as

the angle between the projection of ν_i on the plane perpendicular to Z_i and X_i. We computed these angles for each subunit on 1,061 structures, corresponding to the structures saved every nanosecond of the MD simulation. The stereographic projection of these angles allowed us to perform a model-based cluster analysis using the MCLUST package in R (15), which provides iterative expectation-maximization methods for maximum-likelihood estimation in parameterized Gaussian mixture models. Given as an input the cumulated stereographic projection of polar and azimuthal angles, per subunit, this package provides the number of clusters, the mean position and covariance matrix of each cluster, and the classification, i.e., the relationship between each data point in the stereographic projection and a specific cluster.

Solvent accessible surface area.

(Fig. 4*C*) The VMD built-in *measure sasa* command was used to calculate solvent accessible surface area (SASA) of each residue at every nanosecond. To calculate the values plotted in Fig. 4*C*1 and 4*C*2, SASA were first averaged over the first or last 100 ns and then normalized using the accessible surface of isolated residues in a gly-X-gly environment. Spline fit curves are traced between points. Standard deviations are noted as error bars.

Stabilization energy of ion reservoirs.

(Fig. S6*b*) The ion density was calculated in arbitrary units for z slices of 0.25 Å thickness, with a cylindrical volume calculated using the pore radius of the slice given by HOLE (16). The average density of the bulk was used as the reference state (zero energy). Densities were averaged over 4 successive slices (1 Å total thickness). The relative energy of the reservoirs was calculated using a Boltzmann weighting scheme with a temperature of 300 K.

Normal modes analysis.

Projection of difference vectors between the starting frame ($t = 0$ ns) and snapshots every 100 ns during the simulation was done along low-frequency normal modes derived from the elastic network model. It was consistently observed that only 4–5 among the 10–20 lowest frequency normal modes were sufficient to explain over 90% of the transition.

Electrophysiology.

Cell injection.

Defolliculated, stage 6 (17) *Xenopus laevis* oocytes were obtained from a commercial supplier one day after ovary dissection. DNA (<2 ng) was blind injected into the nucleus through the animal pole, using a pneumatic microinjector, as a mixture in water of GLIC cDNA in a pmt3 vector (0.08 g/L) and green fluorescent protein cDNA in the same vector (0.02 g/L), as a reporter gene for successful intranuclear injection. Identified cells were kept in 96-well plates with U-shaped bottom, in Hepes buffered (18) solution, at 18 °C for two days and then at 15 °C. GFP positive oocytes were used ten days after injection.

Electrophysiological experiments.

Oocytes were superfused with the animal pole facing a gravity-driven solution inflow (4–10 mL/min) in a corridor-shaped recording chamber. A solution of (in mmol/L) NaCl 100, KCl 3, $CaCl_2$ 1, $MgCl_2$ 1, and MES 10 was prepared at pH 8.0 using NaOH. The control extracellular pH (7.3) and lower pH values were then reached by adding HCl 2 mol/L and any extra pH 8.0 solution. The whole oocyte plasma membrane was voltage clamped using two intracellular pipettes filled with 3 mol/L KCl (0.8–1.5 MΩ), and distinct current and voltage-referencing extracellular electrodes bridged to the bath near suction using 3 mol/L KCl filled pipettes (<0.1 MΩ). Currents were recorded at room temperature (21–23 °C), sampled at 500 Hz after low pass filtering (200 Hz), and further filtered using 100 to 1-mean sample data reduction for figure display. Proton dose–response curves were established at a holding potential of −60 mV, using manually controlled 30-s test-pH applications separated by a 30- to 40-s wash at pH 7.3.

1. Kabsch W (1993) Automatic processing of rotation diffraction data from crystals of initially unknown symmetry and cell constants. *J Appl Cryst* 26:795–800.
2. CCP4 (1994) The CCP4 suite: Programs for protein crystallography. *Acta Crystallogr D* 50(Pt 5):760–763.
3. Emsley P, Cowtan K (2004) Coot: Model-building tools for molecular graphics. *Acta Crystallogr D* 60(Pt 12 Pt 1):2126–2132.
4. Murshudov GN, Vagin AA, Dodson EJ (1997) Refinement of macromolecular structures by the maximum-likelihood method. *Acta Crystallogr D* 53(Pt 3):240–255.
5. Blanc E, et al. (2004) Refinement of severely incomplete structures with maximum likelihood in BUSTER-TNT. *Acta Crystallogr D* 60(Pt 12 Pt 1):2210–2221.
6. Davis IW, et al. (2007) MolProbity: All-atom contacts and structure validation for proteins and nucleic acids. *Nucleic Acids Res* 35:W375–383.
7. Bocquet N, et al. (2009) X-ray structure of a pentameric ligand-gated ion channel in an apparently open conformation. *Nature* 457(7225):111–114.
8. Humphrey W, Dalke A, Schulten K (1996) VMD: Visual molecular dynamics. *J Mol Graph* 14(1):33–38, 27–38.
9. Phillips JC, et al. (2005) Scalable molecular dynamics with NAMD. *J Comput Chem* 26(16):1781–1802.
10. MacKerell Jr AD, et al. (1998) All-atom empirical potential for molecular modeling and dynamics studies of proteins. *J Phys Chem B* 102(18):3586–3616.
11. Darden T, York D, Pedersen L (1993) Particle mesh Ewald—An N.log(N) method for Ewald sums in large systems. *J Chem Phys* 98(12):10089–10092.
12. Tuckerman M, Berne BJ, Martyna GJ (1992) Reversible multiple time scale molecular dynamics. *J Chem Phys* 97:1990–2001.
13. R Development Core Team (2008) *R: A Language and Environment for Statistical Computing* (R Foundation for Statistical Computing, Vienna, Austria), http://www.R-project.org.
14. DeLano WL (2002) *The PyMOL User's Manual* (DeLano Scientific, Palo Alto, CA).
15. Fraley C, Raftery AE (2007) Model-based methods of classification: using the mclust software in chemometrics. *J Stat Software* 18(6):1–13.
16. Smart OS, Neduvelil JG, Wang X, Wallace BA, Sansom MS (1996) HOLE: A program for the analysis of the pore dimensions of ion channel structural models. *J Mol Graph* 14(6):354–360, 376.
17. Dumont JN (1972) Oogenesis in Xenopus laevis (Daudin). I. Stages of oocyte development in laboratory maintained animals. *J Morphol* 136(2):153–179.
18. Barth LG, Barth LJ (1959) Differentiation of cells of the Rana pipiens gastrula in unconditioned medium. *J Embryol Exp Morphol* 7:210–222.
19. Law RJ, Lightstone FC (2009) Modeling neuronal nicotinic and GABA receptors: Important interface salt-links and protein dynamics. *Biophys J* 97(6):1586–1594.
20. Krieger E, Nielsen JE, Spronk CA, Vriend G (2006) Fast empirical pKa prediction by Ewald summation. *J Mol Graph Model* 25(4):481–486.

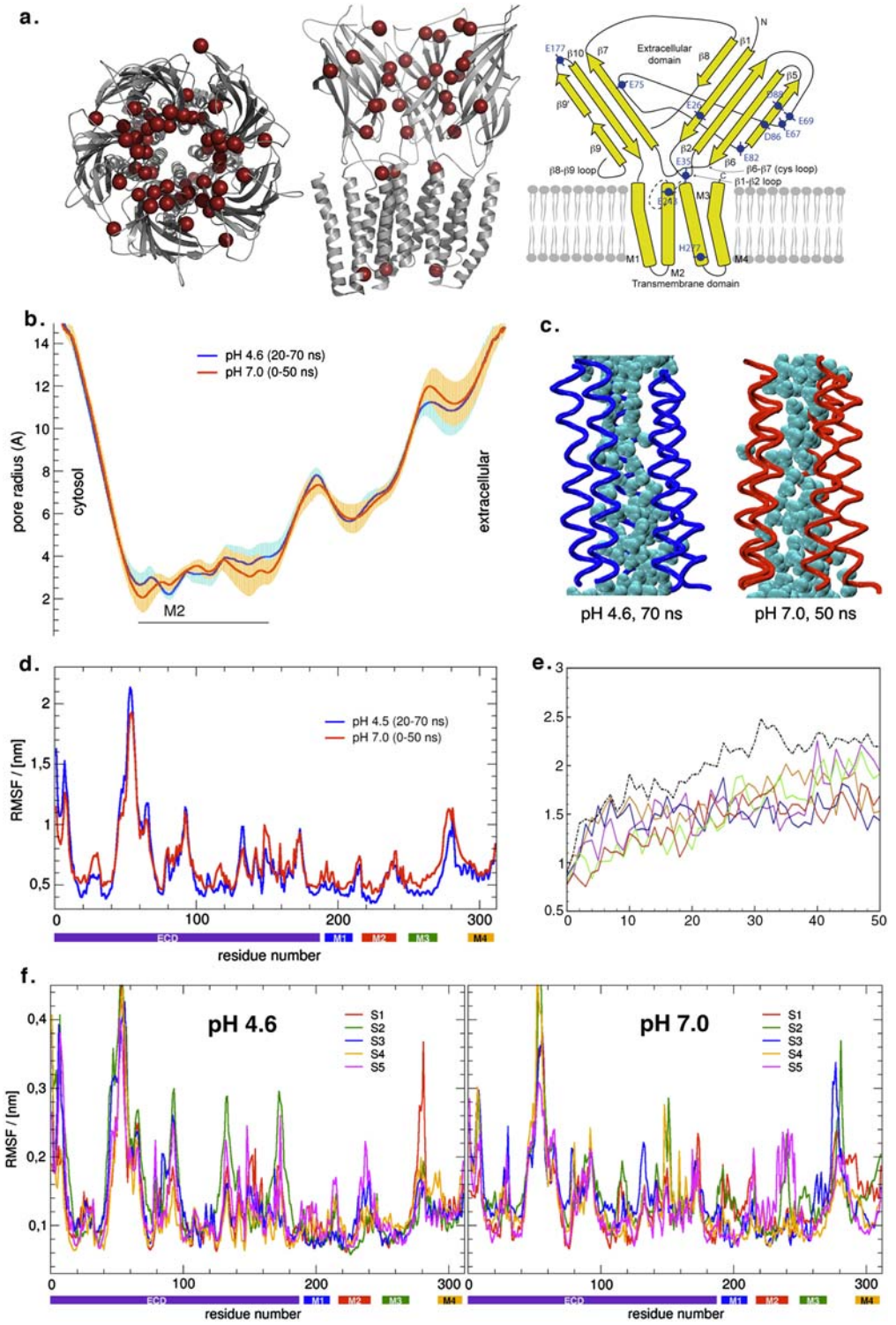

Fig. S1. Open state control simulation (*a*). Charged residues altered by the pH jump. Top and side views of the protein represented as gray ribbons with red spheres indicating the positions of the residues whose protonation states were changed during the pH jump. On the right, location of these residues on a topology scheme. It should be noted that the ECD hosts 9 out of the 11 residues that changed protonation state. (*b*–*e*) Comparison of the control simulation at pH 4.6 (*Blue*) and the production run at pH 7.0 (*Red*) for an equivalent 50-ns period. This control shows that the channel behaves differently at both pH values. *b* shows a pore radius profile comparison, with the simulation at acidic pH showing a higher (more open) profile. *c* illustrates channel hydration after 50 ns. *d* compares cumulated root mean square fluctuations for both simulations, with consistently higher values at pH 7.0. *e* is the structural drift between equivalent frames of the trajectories, for each subunit and overall (*Black Dotted Line*), indicating that the pH switch induces a different evolution of the trajectory, as expected. Concerning this control, we do note that we are still unsure about the right protonation state at acidic pH and are currently investigating this issue. Open state simulations should thus be considered with caution until the protonation state at pH 4.6 is known with confidence. (*f*) Root mean square fluctuations (RMSF) for the simulations at acidic and neutral pH, averaged over a 50-ns period for the main chain atoms. The simulation at pH 7.0 exhibits higher RMSF values than for pH 4.6. Average RMSF is 0.125 vs. 0.108 nm for transmembrane and 0.146 vs. 0.144 nm for extracellular domains, respectively.

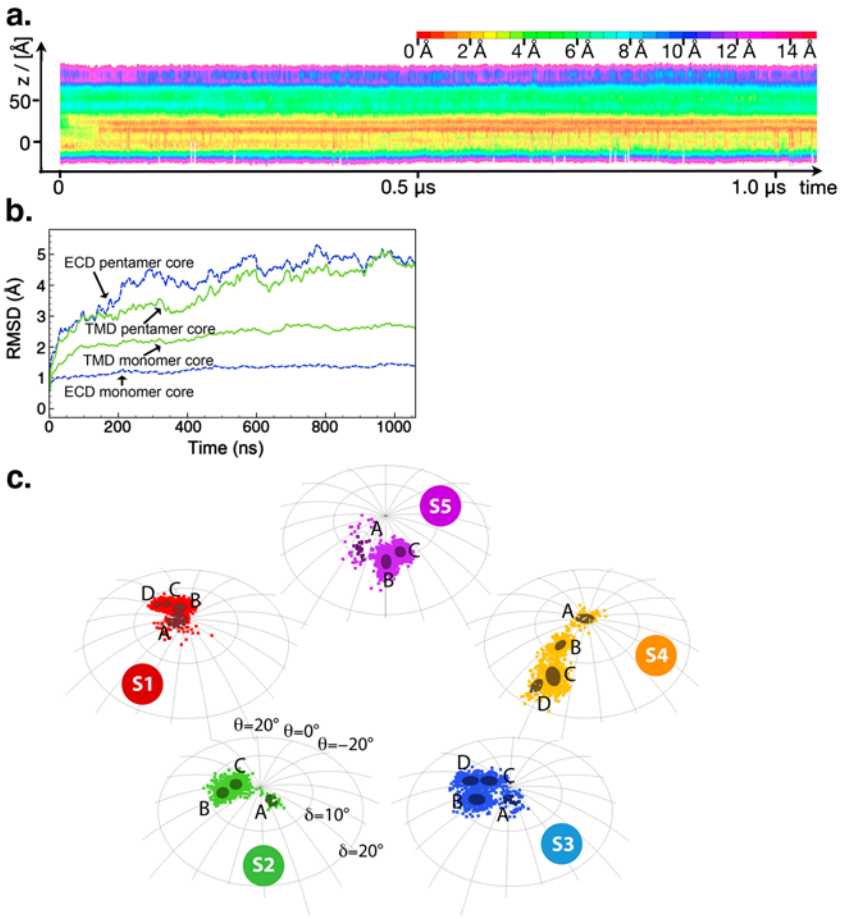

Fig. S2. (*a*) Time evolution of the pore radius profile. Color-encoded plot of the effective pore radius along the channel axis calculated as in the pore profiles of Fig. 2. Color code ranges from constricted (red) to wide open (purple). The color scale bar is shown on top of the graph. The origin of the channel axis is taken at the level of the GLIC T2′ channel constriction, with the extracellular and intracellular ends respectively at the top and bottom of the graph. The molecular dynamics results over the full 1.06-μs production run are presented. (*b*) Rigid body motions of the ECD. Timeline plots of the rmsd between the current frame and the starting point of the production run for the core Cα atoms of the ECD (*Blue Dotted Lines*) and of the TMD (*Green Full Lines*). For each domain, the line with lower rmsd values corresponds to the mean values of the 5 subunits considered separately; the line with higher values corresponds to the pentamer's values. The relatively flat line around rmsd = 1 Å for ECD monomers indicate they undergo little tertiary deformation. The large difference between the two blue lines indicates a clear quaternary rearrangement of the ECDs. This difference is less pronounced for the TMDs. (*c*) M2 helix axes of inertia plotted on spheres. For each subunit, the direction of the principal axis of inertia of the M2 helix, at each nanosecond during the simulation run, is indicated by a point of coordinates δ and θ on a unit sphere. The δ angle measures the inclination of the principal inertial axis of the M2 helix with respect to the direction of the protein symmetry axis. The azimuthal angle θ describes the orientation of the helix in the plane of the membrane (see also Fig. 4*A*). Our convention is that $\theta = 0°$ corresponds to a helix axis oriented toward the pore center. Along the simulation, every helix passes through several stationary positions, often sequentially, which we identified as clusters (see *Trajectory analysis* for details) named A to C or D and highlighted in dark colors.

Analysis of results. The plots shown here in *c* and in Fig. 4*A* display the trajectories defined by following δ and θ angles of each M2 helix, as seen from the extracellular region. Clusters are not equivalent from one subunit to the other, though correlations exist both spatially and temporally. "A" clusters for subunits S1–S4 correspond to mostly vertical helices, with a δ angle of less than 5°. "B" clusters are equivalent for S1 and S2. The S5 "C" cluster is very similar to the S4 "B" cluster and also similar to the S3 "C" and "D" clusters. As can be seen in Fig. 4*B*, which displays a timeline of cluster occupation, switches from one cluster to the other are often synchronous between subunits. Two major events can be distinguished. All M2s leave their initial positions ("A" cluster) after about 0.05 μs of simulation and rotate clockwise around the pore axis. They do so without rotating on themselves, except for S5, which experiences a rotation of about 10° (data not shown). This rotation exposes some previously buried residues such as F238 to the pore axis. The second main event occurs between 0.4 and 0.6 μs of simulation. The M2 of S5 leaves its "C" cluster to occupy "B," further swinging into the pore with an inclination δ of about 10°. At the same moment, S4, the immediate neighbor of S5 that was in a position equivalent/symmetric to S5, leaves its "B" cluster for cluster "C," continuing its initial move. It reaches a δ angle of about 15° with the membrane normal direction, θ being 40° away from the pore toward subunit S3. This second event leads to S3 reaching its "C" and "D" clusters, corresponding to a minor inclination δ of 5 to 8°, and θ around 45° from the pore (compared to more than 80° in the first phase) toward S2. This second event has very little effect on the S2 M2 helix, but, interestingly, while the trend for every helix is to tilt its upper part toward the pore, S1, the other immediate neighbor of S5, clearly moves away from it. Overall, the motions of the M2 helices along this one microsecond run appear asymmetric but concerted.

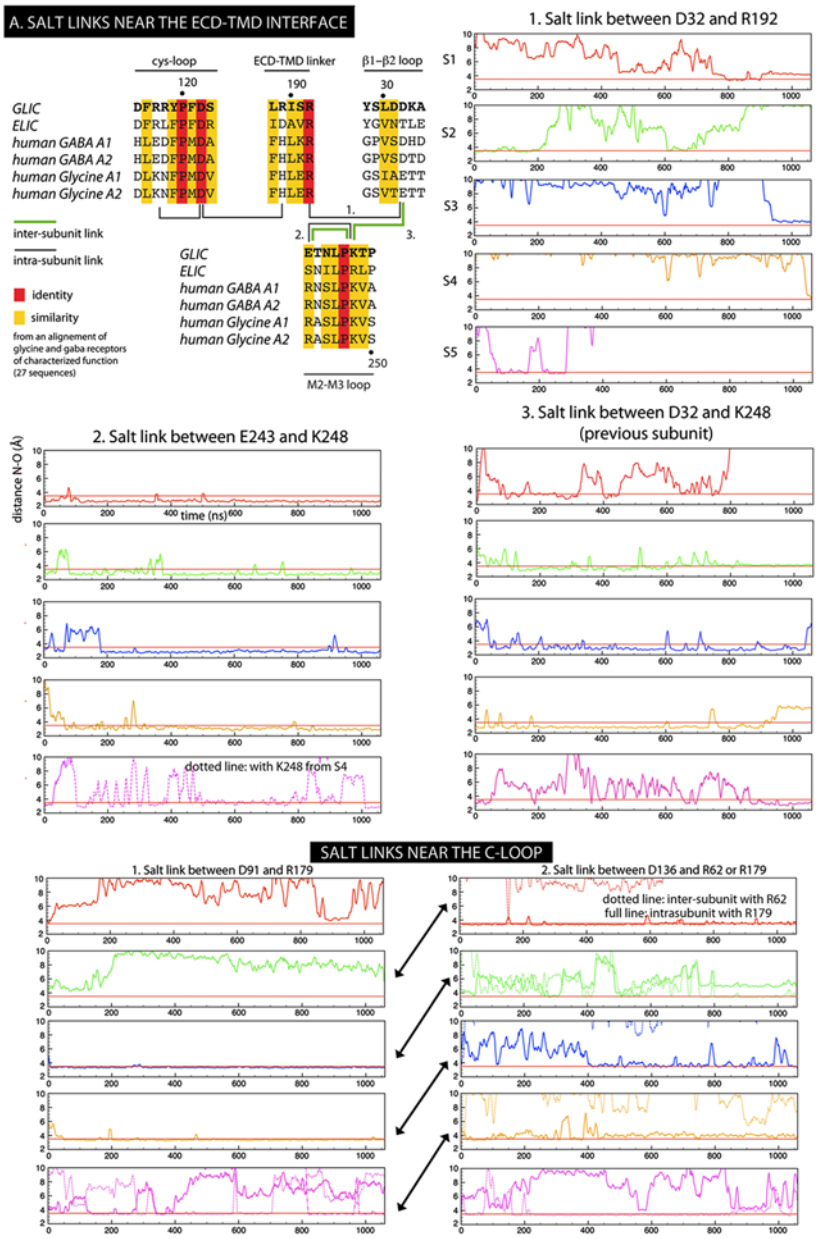

Fig. S3. Salt bridges. (*A*) Salt links near the ECD–TMD interface. Part of a sequence alignment between GLIC, ELIC, and GabaA or glycine CLRs is given. Only the loops at the interface between the membrane and the extracellular domain are shown. Salt bridges existing during the simulation run are indicated by black (intra-) or green (inter-) subunit lines. (1, 2, and 3) Timelines of nitrogen to oxygen distances between charged pairs for residues D32-R192, E243-K248, and D32-K248, respectively. A separate plot is provided for each subunit, with the same color code as in the rest of the manuscript. (*B*) Salt links near the C loop using the same timeline representations for D91-179 (1) and D136-R62/R179 (2).

Analysis of results: Salt links bridging two different subunits or bridging ECD and TMD were examined. Overall, we note that about ten salt links may transiently exist at each interface and that the more stable bridges occur at two discrete positions along the pore axis, previously pointed out for their importance in gating: at the level of the C loop and of the β1–β2 and M2–M3 loops (19). Salt links bridging two different subunits or bridging ECD and TMD were examined. Distances between oxygen atoms of carboxylic acids and nitrogen atoms of basic residues were measured [using the Salt Bridge plugin of VMD (8)] and the pairs for which those distances were below 3.5 Å were kept. The conserved acidic D32 residues from the β1–β2 loop form a very stable salt bridge with K248 in the adjacent subunit's M2–M3 loop. For two of the subunit–subunit interfaces, the D32–K248 bridge is present more than 80% of the time, for the remaining three interfaces more than 35%. This interdomain, intersubunit link is a unique feature in our simulation: No other interdomain bridge is found. In the GLIC crystal structure, D32 is involved in a structural salt bridge with R192 (belonging to the ECD–TMD linker), which holds the two β-sheets of the sandwich together. This bridge is also detected in the early parts of the simulation, mostly before 0.25 μs. It is present up to 15% of the time for two of the subunits. When K248 does not contact D32, it can be involved in a stable link with E243 from the M2 helix. For subunits S1–S4, this link exists for ∼90% of the simulation time. Only E243 in subunit S5 can form a link with its neighbor K248, in line with the unique behavior of the upper part of M2 in this subunit. In the crystal structure, no intra- or intersubunit salt bridges are observed between these residues. On the contrary, in the neighborhood of the binding pocket in eukaryotic CLRs, two intersubunit links are found in the open structure: D91-R179 and D136-R62. The first one is partly conserved during the simulation in S2–S3 and S3–S4 for more than 84% of the time. D91-R179 is however hardly present in S1–S5, for instance. In S5, D91 is in contact with R179 of S4 at the beginning of the simulation until ∼0.25 μs. Then it switches to R133 of the same neighbor and finally reaches R62 of its own subunit after 0.7 μs. Only for S2–S3 and S1–S5 does the D136-R62 link exist for a significant time. D136 can also be engaged in an intrasubunit salt bridge with R179.

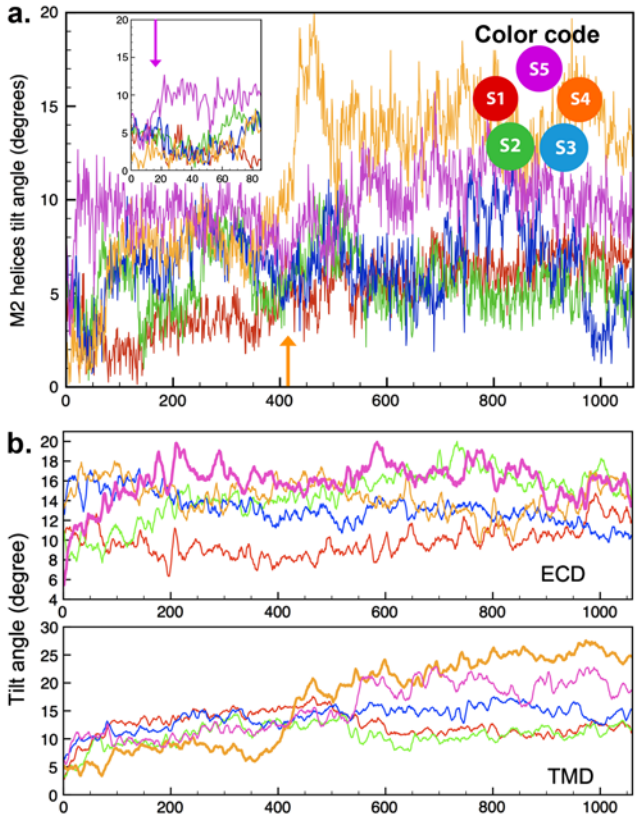

Fig. S4. Events timeline. (*a*) Polar (tilt) angles for M2 helices in the first 100 ns (*Inset*) and for the whole simulation. Arrows indicate two crucial events, for S5 around 25 ns and for S4 around 400 ns. These events correspond respectively to motions from cluster A to B for S5 and B to C for S4 as described in the main text and Fig. 4*B*. (*b*) Tilt angles of the principal axis of inertia (same definition as δ in Fig. 4) for the ECD and TMD domains, for each subunit.

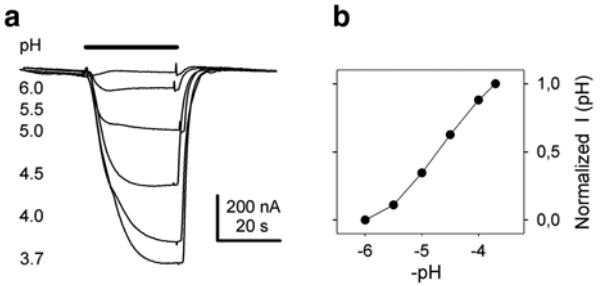

Fig. S5. GLIC A13′F mutant is functional. (*a*) Superimposed currents recorded from a *Xenopus* oocyte expressing the A13′F GLIC mutant, before, during, and after 30-s applications of extracellular solutions of various pH values, as indicated left to the traces. Control pH value for washing solutions is 7.3. Holding potential is set at −60 mV. (*b*) Corresponding dose–response curve. The maximum current deviation within 30 s was measured at each pH and normalized to its value at pH 3.7. Each point is the average of three independent measurements.

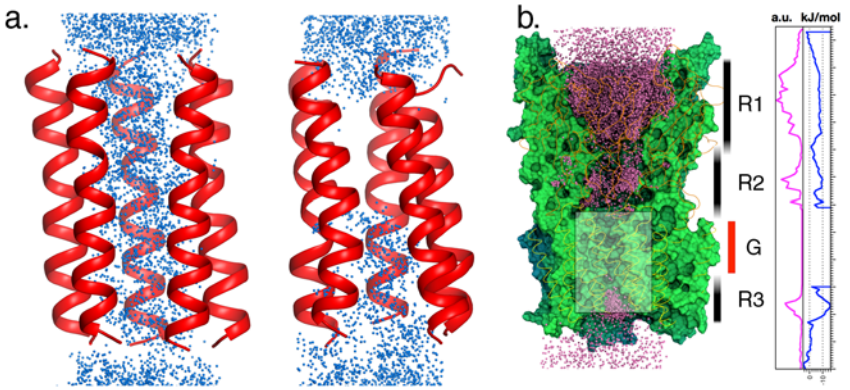

Fig. S6. GLIC channel hydration and cation reservoirs. (*a*) Cumulated views of the water density in the ionic channel at the beginning (*Left*) and end (*Right*) of the simulation, respectively. All observed water positions during a 20-ns interval are depicted as blue dots. The transmembrane M2 helices are shown as red ribbons. This view is a zoom of the rectangle represented in *b*. (*b*) Cation reservoirs detected during the simulation. Cation densities are depicted as pink dots. The locations of reservoirs R1–R3 and of the cation free gating region G are indicated. The molecular surface of a cross-section of the whole protein is shown. On the right, the ion density is shown in arbitrary units (*Pink*). The blue curve illustrates an estimation of the energy of the cation basins with respect to bulk.

Analysis of results: Channel hydration was analyzed by accumulating the positions of all water molecules in a 20-ns window at the beginning and end of the simulation (Fig. S3*a*). This analysis confirms that the simulation initially samples an open-like state, with a continuous water column enabling permeation of ions across the channel. This water column is disrupted in the upper half of M2 early on in the simulation, at about 0.07 μs until the end. Movie S1 illustrates this process. The loss of channel hydration underlines the presence of a hydrophobic gate in this region and confirms that the receptor is fully closed. Fig. S3*b* illustrates which parts of the channel pore are visited by cations. Interestingly, cations are attracted by the channel and accumulate within three distinct reservoirs (R1–3), with an entirely cation-free gating region (G). The cation density along the channel axis can be used to estimate the stabilization of the ions within the reservoirs compared to bulk. The highest −15 kJ/mol stabilization is observed for R3, the smallest of the reservoirs. The larger reservoirs R1 and R2 are stabilized by about −8 and −10 kJ/mol, respectively.

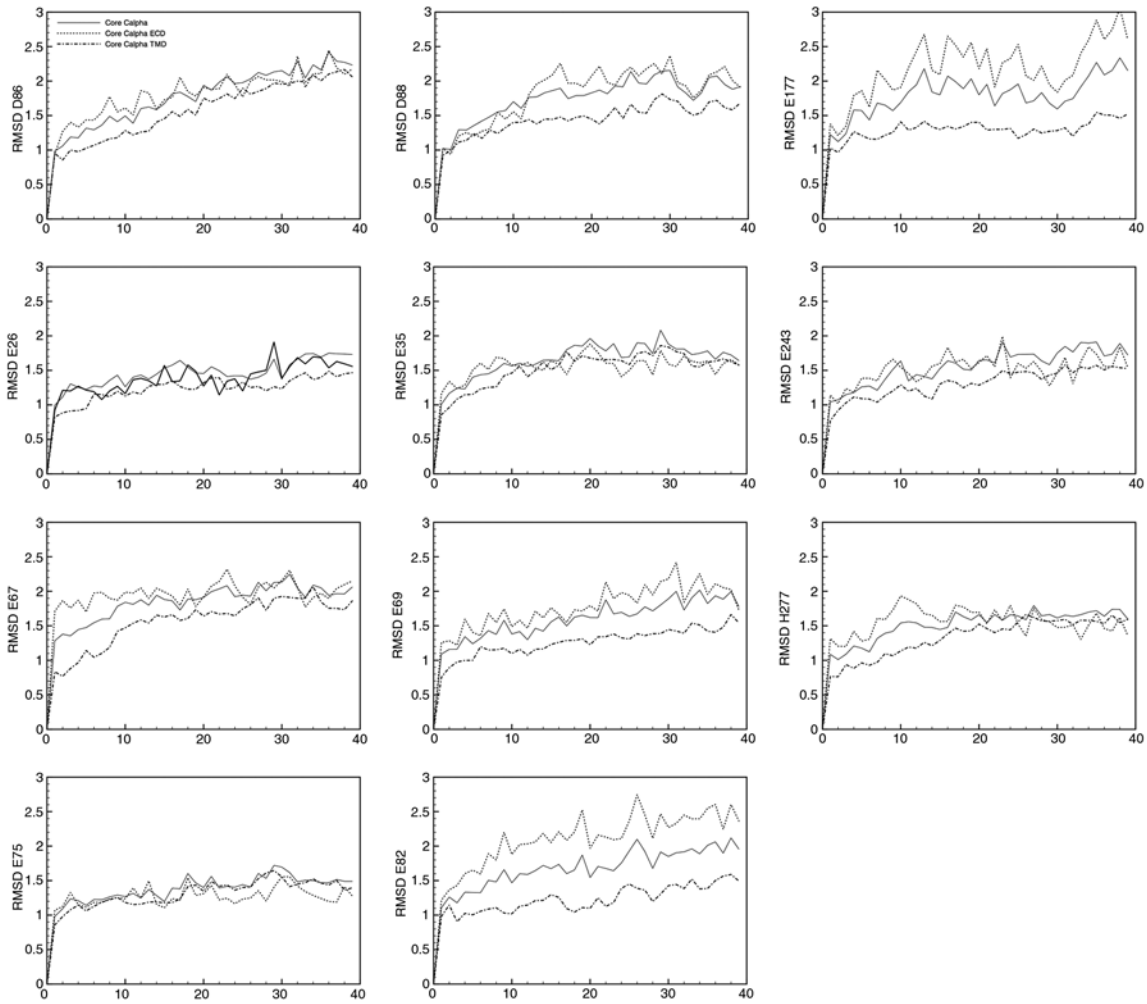

Fig. S7. Individual protonation state change rmsd for 20-ns control simulations switching each of the suspected ionizable residues individually. The plain black line indicates overall rmsd, the dotted line is for the transmembrane, and the broken line for the extracellular domain. The *y* axis represents rmsd in Å and the *x* axis the frame number taken every 500 ps.

Table S1. Protonation state changes adopted

Residue	Average pK_a*
GLU 26	5,1
GLU 35	4,8
GLU 67	5,0
GLU 69	5,0
GLU 75	5,0
GLU 82	4,7
ASP 86	4,9
ASP 88	5,0
GLU 177	4,9
GLU 243	4,6
HIS 277	5,4

*Average predicted pK_a for residues with more than 50% probability of being protonated by changing pH from neutral to pH = 4.6. These predictions were made with the Yasara software (20) based on the GLIC crystal structure (Protein Data Bank ID 3EAM). Averages were calculated from equivalent symmetry-related residues. Several other residues are in a "twilight zone" with around 50% probability of being protonated. These were kept in their standard protonation state in the current seeding simulation at acidic pH. It has to be emphasized that this protonation state at pH 4.6 should be considered as a working hypothesis but is in no way a resolved issue. We are still unsure about the right protonation state at acidic pH and are currently investigating this issue further.

Table S2. Data collection and refinement statistics

Dataset	A13′F mutant
Beamline	European Synchrotron Radiation Facility id23eh1
Wavelength (Å)	1.07
Space group	C2
Unit cell (Å)	181.73 133.01 159.90 $\beta = 102.89$
Resolution (Å)	25–3.15 (3.32–3.15)*
R_{merge} (%)	15.3 (60.0)*
Completeness (%)	99.6 (99.9)*
$\langle I/\sigma \rangle$	10.4 (2.3)*
Observed (unique) reflections	239,855 (64,368)
Redundancy	3.7 (3.8)*
Refinement statistics	
Resolution (Å)	20–3.15
Reflections working set (test set)	62,602 (3193)
R_{cryst} (R_{free}) (%)	21.5 (22.4)
Non-H protein (ligand) atoms	12,666 (111)
⟨B factors⟩ (Å^2)	56.8
rmsd	
Bond lengths (Å)	0.010
Bond angles (degrees)	1.2

*Values for the highest resolution shell.

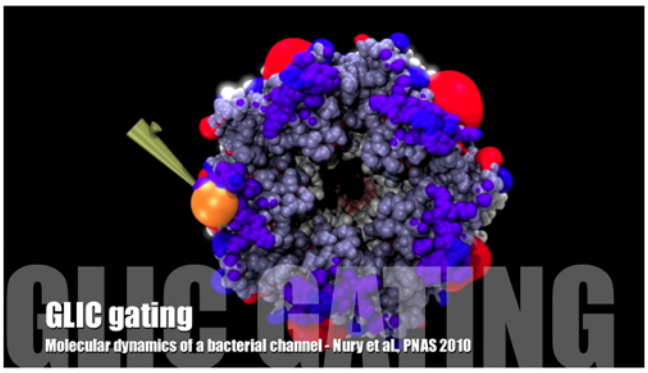

Movie S1. A movie of the 1.0 μs simulation including a view of the water channel disrupting.

Movie S1 (MOV)